8 Muon identification and measurements

A robust muon identification and high precision momentum measurement is crucial to fully exploit the physics potential of the LHC. The muon energy of physics interest ranges over a large interval from a few GeV, *e.g.* for *B*-physics studies (see Chapter 17), up to a few TeV, where one might expect the presence of new physics (see *e.g.* Chapter 21).

From the point of view of muon detection, the ATLAS apparatus is characterised by two high precision tracking systems, namely the Inner Detector and the Muon System, and a thick calorimeter that ensures safe hadron filtering with high purity for muons of momentum above 3 GeV. In this chapter, the methods for combined reconstruction using these subdetectors and their physics performance are described.

The combination of measurements made in the Muon System with the ones from the Inner Detector improves the momentum resolution in the momentum range 6 GeV $< p_T <$ 100 GeV; this is described in Section 8.1. The matching of the muon track reconstructed independently in the Inner Detector and in the Muon System also allows the rejection of muons from secondary interactions as well as the ones from π/K decays in flight, as described in Section 8.3. The combined reconstruction allows efficient identification of muons inside jets with low hadron misidentification as shown in Section 8.4. Low energy muon identification is possible thanks to the hadron calorimeter; indeed, low rapidity muons with momentum above 3 GeV can be efficiently identified in the outer sampling of the calorimeter; this is described in Section 8.2. The measurement of the activity around the muon track is important to discriminate between processes where isolated muons are produced and background reactions where muons are produced by the semileptonic decay of *b*- and *c*-quarks, as presented in Section 8.5. The excellent momentum resolution and reconstruction efficiency lead to good multi-muon mass reconstruction (see Section 8.6), which in turn allows tight event selection and hence strong background rejection.

8.1 Track measurement combination

In this section the methods to combine tracks from the Inner Detector and the Muon System are described. The combined performance has been evaluated with single muons of fixed transverse momentum. The analysis shows a high reconstruction efficiency for high transverse momenta. Muons with $p_T <$ 6 GeV are difficult to identify in the standalone Muon System, in particular in the barrel. The use of the Tile Calorimeter is mandatory for the identification of low p_T muons produced at small rapidity.

8.1.1 Track combination procedures

In order to combine the tracks reconstructed in the Inner Detector and the Muon System, two complementary strategies were considered. The first strategy is based on the statistical combination of two independent measurements using the parameters of the reconstructed tracks and their covariance matrices. This method is used in the STACO procedure. The second strategy consists in fitting the global muon track using the hits from the two subdetectors which were found and used separately by the standalone reconstructions. This strategy was used in the MUID and COBRA procedures.

8.1.1.1 STACO

The principle of the STACO method is the statistical combination of two independent measurements by means of their covariance matrices. For two tracks on some reference location defined by their parameter vectors, P_1 and P_2, and their covariance matrices, C_1 and C_2, the parameter vector of the combined track, P, is the solution of the equation

$$\left(C_1^{-1} + C_2^{-1}\right) \times P = C_1^{-1} \times P_1 + C_2^{-1} \times P_2.$$

Its covariance matrix, C, is given by

$$C = \left(C_1^{-1} + C_2^{-1}\right)^{-1},$$

and the corresponding χ^2 is given by

$$\chi^2 = (P - P_1)^T \times C_1^{-1} \times (P - P_1) + (P - P_2)^T \times C_2^{-1} \times (P - P_2).$$

In the present implementation of the STACO procedure, the combination is done at closest approach to the beam line in the perigee representation using track measurements performed in the Inner Detector and the Muon System. The track reconstruction in the Inner Detector is performed by the xKalman package [8-1] and the track reconstruction in Muon System is performed by the MUONBOX package [8-2] using the reconstructed track parameters expressed at the Inner Detector exit. The corrections for energy loss in the calorimeters are done in MUON-BOX using a momentum dependent parametrisation and a detailed geometrical description of the detector outside the Inner Detector exit; in addition the effects of multiple scattering and energy losses fluctuations have been taken into account in the covariance matrix propagation. The track is then propagated down to the closest approach to the beam line accounting for multiple scattering effects in the Inner Detector.

Initially, the track combination is tried only for pairs of tracks that show a reasonable matching in the (η, ϕ) plane. Then the track combination is accepted only if the global χ^2 is below a maximal value. When different combinations are possible, a simple algorithm has been applied to solve the ambiguities. The pair giving the best combined χ^2 is retained and the corresponding tracks are removed from the initial samples of the tracks to be combined. The same procedure is then applied until no more combination is possible.

8.1.1.2 MUID

The MUID muon identification package combines Muon System tracks reconstructed by MUONBOX with Inner Detector tracks found using the iPatRec package [8-3]. The principle is to use the hits found in the two subsystems with information from the calorimeters. The purpose of MUID is to identify Inner Detector tracks as muons at all momenta, to obtain improved parameter resolutions at intermediate momenta, and to clip the tails of badly measured high momentum muons (such as those resulting from catastrophic bremsstrahlung and the pattern recognition errors caused by showering in the Muon System).

The first step is to re-express tracks from the Muon System in order to have the same representation as those from the Inner Detector reconstruction. The muons are propagated through the magnetic field with energy loss and multiple scattering contributions included to obtain the pa-

rameters with their covariance at the point of closest approach to the intersection region. This is performed by applying the iPatRec track fitter to a set of scattering planes representing the calorimeter and Muon System material, an energy loss 'measurement' obtained either from the observed calorimeter energy deposition or from parametrisation, and to either the MUONBOX fit parameters given at the entrance of the Muon System or the drift and strip hits assigned by MUONBOX. Currently, the alternative treatments of the Muon System data are essentially equivalent at high energy, whereas at low p_T the error propagation works better in the region of high field gradient. The results presented in this chapter have been obtained using this latter option. It is hoped that the use of the hits will improve the performance in some cases such as badly-measured muon phi-coordinates, and enable an extension to use segments from the first barrel station to improve the low p_T efficiency.

In the next step, tracks are matched by forming a χ^2 with 5 degrees of freedom from the parameter differences and summed covariances. A combined fit is performed to all matches with χ^2 probability above 0.001. When no match satisfies this criterion, a combined fit is attempted for the best match within a road around the muon track. The combined fit is a repeat of the muon fit from the first step with the addition of the Inner Detector hits and scattering planes assigned by iPatRec. Finally all matches to the Inner Detector giving a satisfactory combined fit are retained as identified muons.

For isolated muons the energy loss is taken from the associated calorimeter cells. It is corrected as a function of η and momentum to account for the difference between true and observed energy deposition obtained from the simulation. Typically this correction increases the energy loss correction by about 7%. The benefit of this procedure over parametrisation is to better correct for Landau fluctuations, in particular at intermediate energies where the calorimeter energy loss is significant and the Muon System gives a more precise momentum measurement than the Inner Detector. At low momentum the precision is comparable to that from parametrisation, but here the purpose of the combined fit is to identify the track as a muon rather than to improve the parameters measured by the Inner Detector. Near the threshold for penetration into the Muon System, the calorimeter energy deposition is greater than the remaining track momentum, thus the measured energy provides a valuable consistency check not available from parametrisation. A parametrised correction is used for non-isolated muons. The MUID package is still under development and further improvement in performance can be expected.

8.1.1.3 COBRA

The COmBined Reconstruction for Atlas or COBRA package incorporates the average tracking and error propagation of the GEANE package [8-4]. In doing so, COBRA can access the description of the material and the ATLAS magnetic field as used by the GEANT simulation program, thus allowing for an accurate detector description in the reconstruction phase and preventing any inconsistency with the simulation.

COBRA runs after the Inner Detector and Muon System pattern recognition programs. The tracks identified by the two subsystem reconstruction program are extrapolated to a common point, typically the inner surface of the calorimeter or the vertex, correcting for energy loss and updating the covariance matrix along the trajectory. The global reconstruction is performed by calculating the χ^2 probability of the track parameters at this point that results from the combination of track pairs from the two subsystems. After a successful combination, a global refit follows. The refit is a Billoir-like fit, usually called Kalman filter [8-5].

Encouraging results have been obtained so far with the extrapolation, combination and global refit procedure. Development is still in progress and it was not possible to use the package for the studies presented in this chapter. Final results and performance will be published in a separate report [8-6].

8.1.2 Performance

The performance of the methods described above is studied for single muons samples of fixed transverse momenta p_T. The high p_T and low p_T results are shown separately.

8.1.2.1 High p_T muons

In Figures 8-1 and 8-2, distributions of the pull of the inverse of the transverse momenta of the combined tracks obtained using the STACO and MUID procedures are presented for $p_T > 10$ GeV. The pull is defined here as the difference between the reconstructed and true values normalised to the error on the reconstructed value. The fact that the width of these distributions remains close to unity from $p_T = 10$ GeV up to $p_T = 500$ GeV shows that the combination procedures works well over a large p_T range.
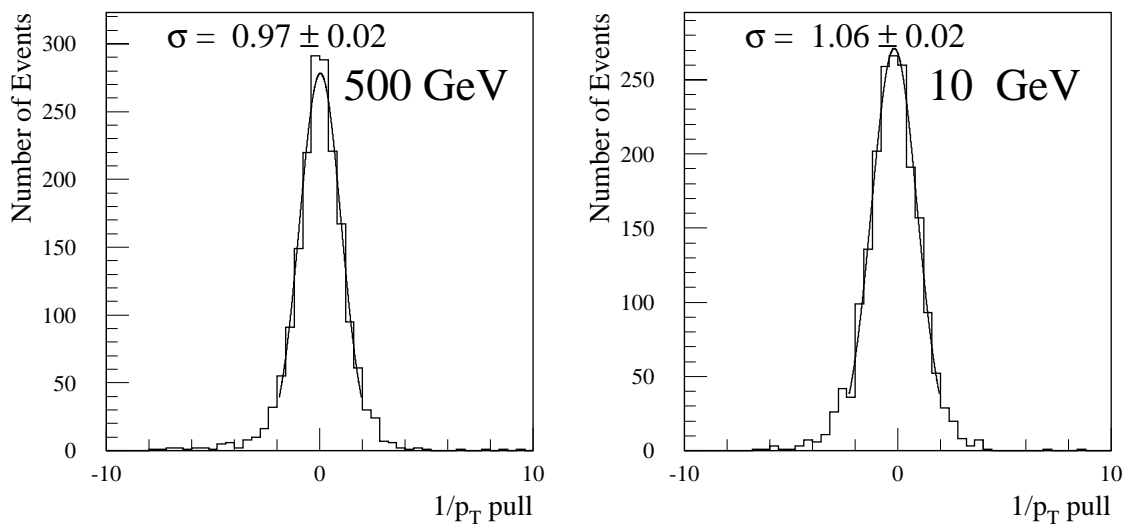
Figure 8-1 Pull distributions of the inverse of the transverse momentum of the combined track using the STACO procedure.

The reconstruction and combination efficiencies and the p_T resolutions are presented in Figures 8-3, 8-4, 8-5 and 8-6 for the full p_T range. The p_T resolutions behave as expected over the whole range: the Inner Detector and the Muon System measurements dominate the combined transverse momentum measurement below 10 GeV and above 100 GeV, respectively. Above 10 GeV, the combination efficiency is high. One notes a slow decrease of this efficiency with increasing p_T from about 97% at 10 GeV down to about 85% at 1 TeV. This decrease, although much less pronounced, is also apparent in the standalone Muon System reconstruction efficiency (from about 98% to about 95%). This behaviour is explained by the increasing (with the muon momentum) probability of occurrence of electromagnetic shower production along the muon track when crossing dense materials. These local showers can create a large number of hits in the Muon System chambers that mask or spoil the genuine muon hits. The lack of meas-
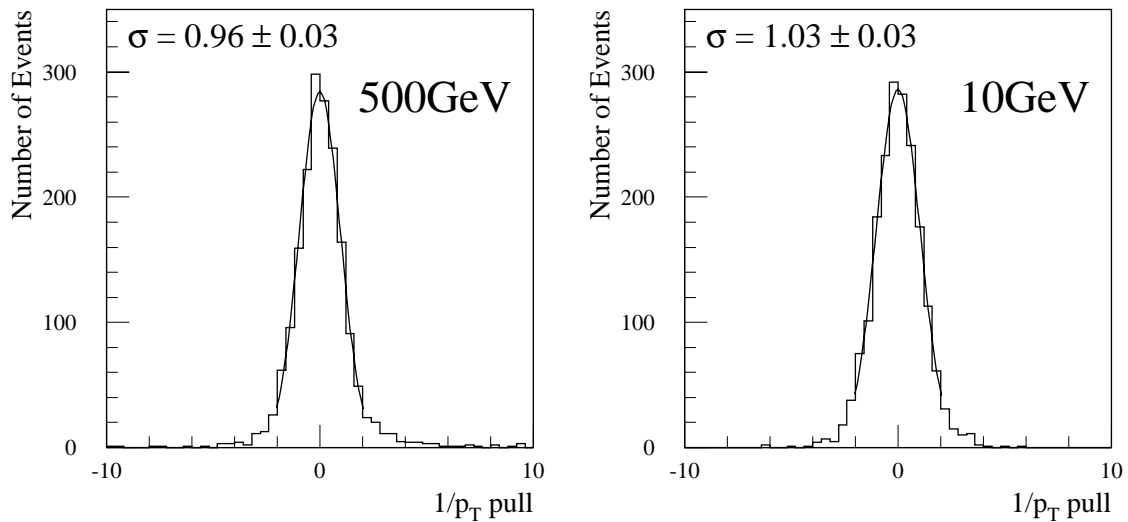
Figure 8-2 Pull distributions of the inverse of the transverse momentum of the combined track using the MUID procedure.

urement redundancy resulting from a cost optimisation (there are only three layers of tubes per multi-layer in the middle and outer stations [8-9]), results in a degradation of the pattern recognition in the Muon System. Some tracks are irretrievably lost leading to an inefficiency of the standalone reconstruction of 5% at 1 TeV. The momentum of some of the reconstructed tracks is spoiled leading to an inefficiency of the combination procedure of order 5% at 1 TeV. This indicates the ultimate reconstruction efficiency of about 90% at 1 TeV.

The remaining 5% needed to account for the observed 85% combination efficiency at 1 TeV comes from pattern recognition errors on transverse position of the reconstructed tracks in the Muon System. It has been shown that a fraction of these tracks have a good momentum measurement but are slightly shifted in the transverse plane. In these cases, the electromagnetic showers have spoiled the hit pattern in the second-coordinates chambers. These tracks could be recovered in the combination procedure by simply increasing the angular errors. The momentum being correctly measured in the Muon System, and the angular measurements being dominated by the Inner Detector measurements, this procedure should be justified; it is under study.

8.1.2.2 Low p_T muons

The reconstruction and combination efficiencies and p_T resolutions for low p_T single muons are presented in Figures 8-7, 8-8, 8-9 and 8-10. As expected, the p_T resolution is completely dominated by the Inner Detector measurements. With respect to high p_T muons, the most important difference concerns the efficiency which decreases very rapidly with decreasing p_T. The combination efficiency follows closely the standalone Muon System reconstruction efficiency and decreases down to about 30% at 3 GeV.

Figures 8-11 and 8-12 illustrate the reasons for this decrease. Accurate tracking of low p_T muons in the highly inhomogenous magnetic field is delicate and requires a dedicated algorithm. Furthermore, the importance of multiple scattering in the Muon System superstructures is enhanced at low p_T and is one of the main reasons for the complexity of the pattern recognition. As p_T decreases, the energy lost by the muons inside the calorimeters becomes comparable to their energy, specially in the barrel region. Therefore, an increasing fraction of the muons exit from the calorimeters with too low energy an to reach the medium or outer muon stations, or do
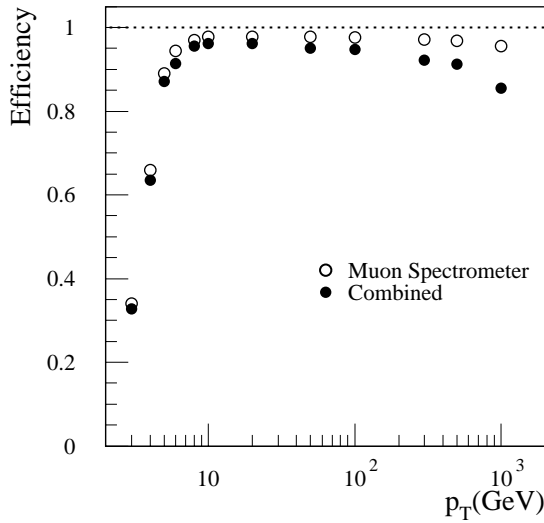
Figure 8-3 Efficiency of tracks reconstruction in the Muon System and of track combination using the STACO procedure as a function of p_T.
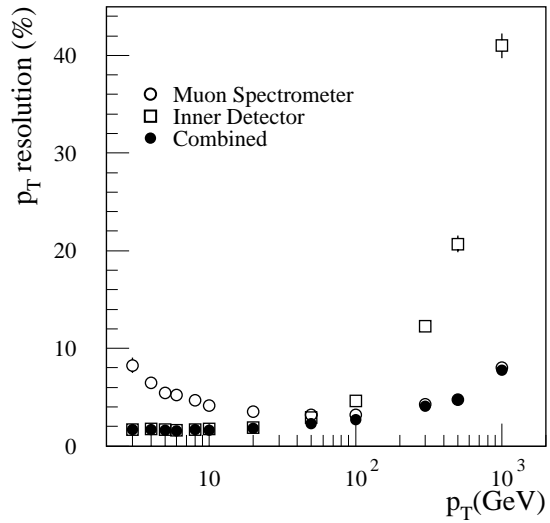

Figure 8-4 p_T resolution of track reconstruction in Muon System, in Inner Detector and of combined tracks using STACO procedure as a function p_T.
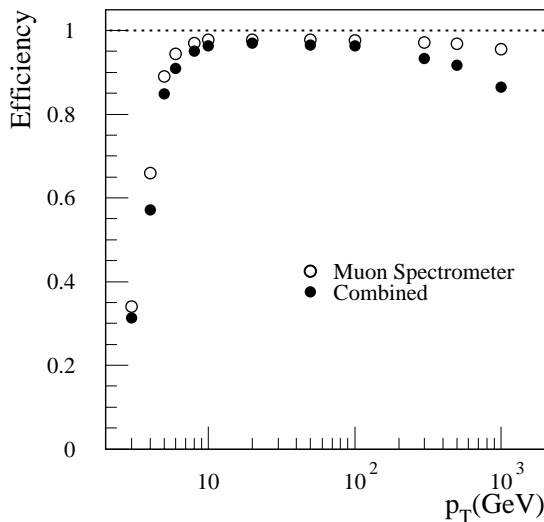

Figure 8-5 Efficiency of track reconstruction in the Muon System and of track combination using the MUID procedure as a function of p_T.
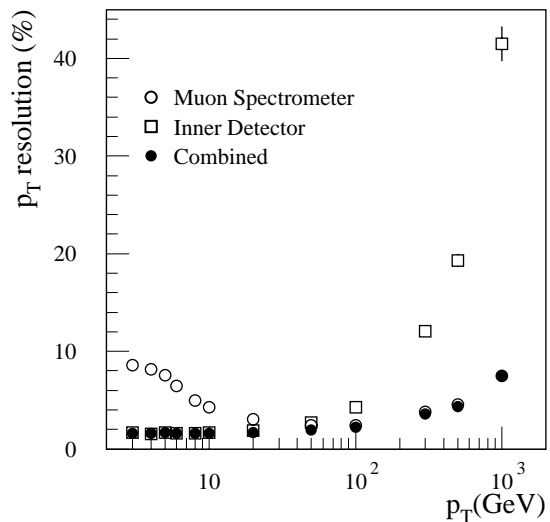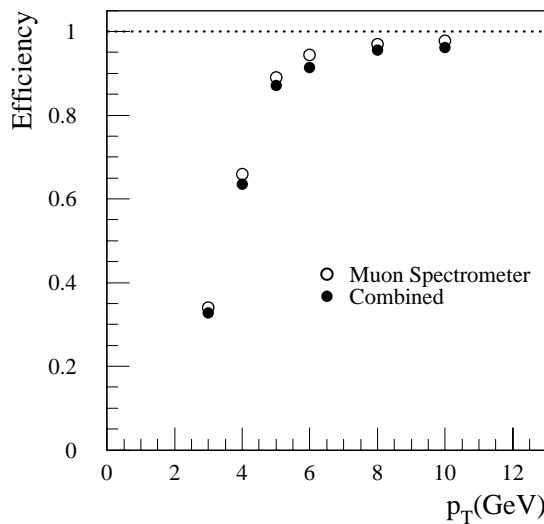

Figure 8-6 p_T resolution of track reconstruction in Muon System (refitted), in Inner Detector and of combined tracks using MUID procedure as a function p_T.

not escape from the calorimeters. Figures 8-11 and 8-12 show that the inefficiency is indeed mainly visible in the barrel region. In the end cap region, even at transverse momentum as low as 3 GeV, the efficiency remains high since the momentum is larger than the 3-4 GeV energy deposited in the calorimeters.

In the absence of a reconstructed track in the Muon System, it is possible to use the straight track segments which can be reconstructed in the inner stations of the Muon System and are made available by the standalone reconstruction program. Figure 8-13 shows the fraction of single muon events with a reconstructed inner station segment as a function of η compared with the standalone reconstruction efficiency. The figure shows that in the high η range, $|\eta| > 1.6$, the

Figure 8-7 Efficiency of track reconstruction in the Muon System and of track combination using the STACO procedure as a function of p_T.
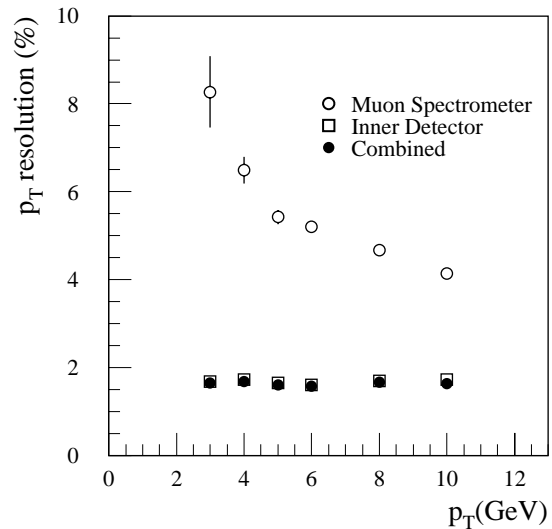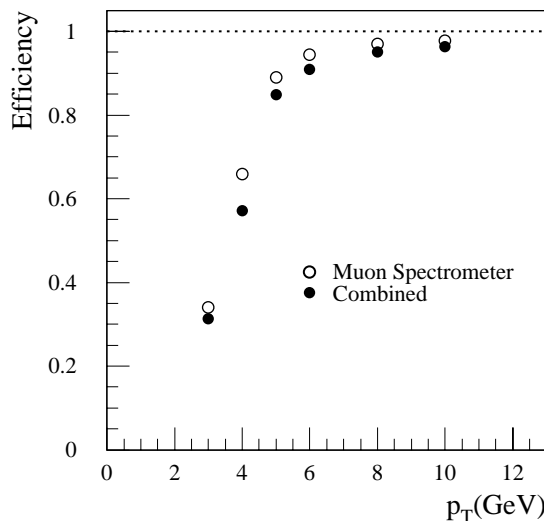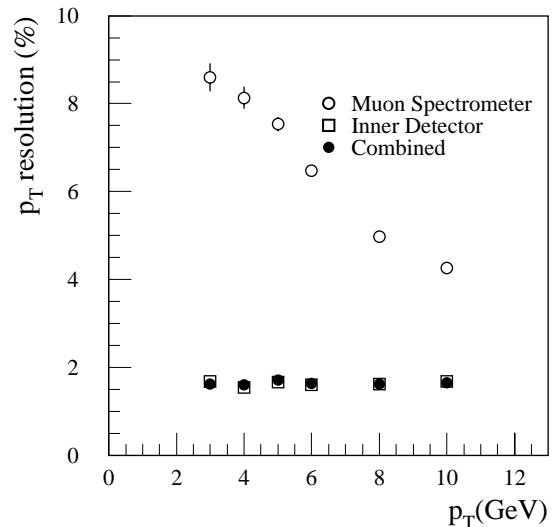

Figure 8-8 p_T resolution of track reconstruction in Muon System, in Inner Detector and of combined tracks using STACO procedure as a function p_T.

Figure 8-9 Efficiency of track reconstruction in the Muon System and of track combination using the MUID procedure as a function of p_T.

Figure 8-10 p_T resolution of track reconstruction in Muon System (refitted), in Inner Detector and of combined tracks using MUID procedure as a function p_T.

identification efficiency will be marginally increased by using the inner station segments. In the intermediate η range, $1.0 < |\eta| < 1.6$, the use of inner station segments could improve the identification efficiency up to about 90%.

Figure 8-13 seems to indicate that a similar gain can be obtained in the barrel region. In this latter region, the inner stations segments suffer from a very imprecise measurement in the direction along the tubes of the precision chamber because of the absence of second-coordinate chambers in the inner stations. This could lead to a high ambiguity in the association of the inner stations segments to the Inner Detector tracks. An algorithm that uses the inner station seg-
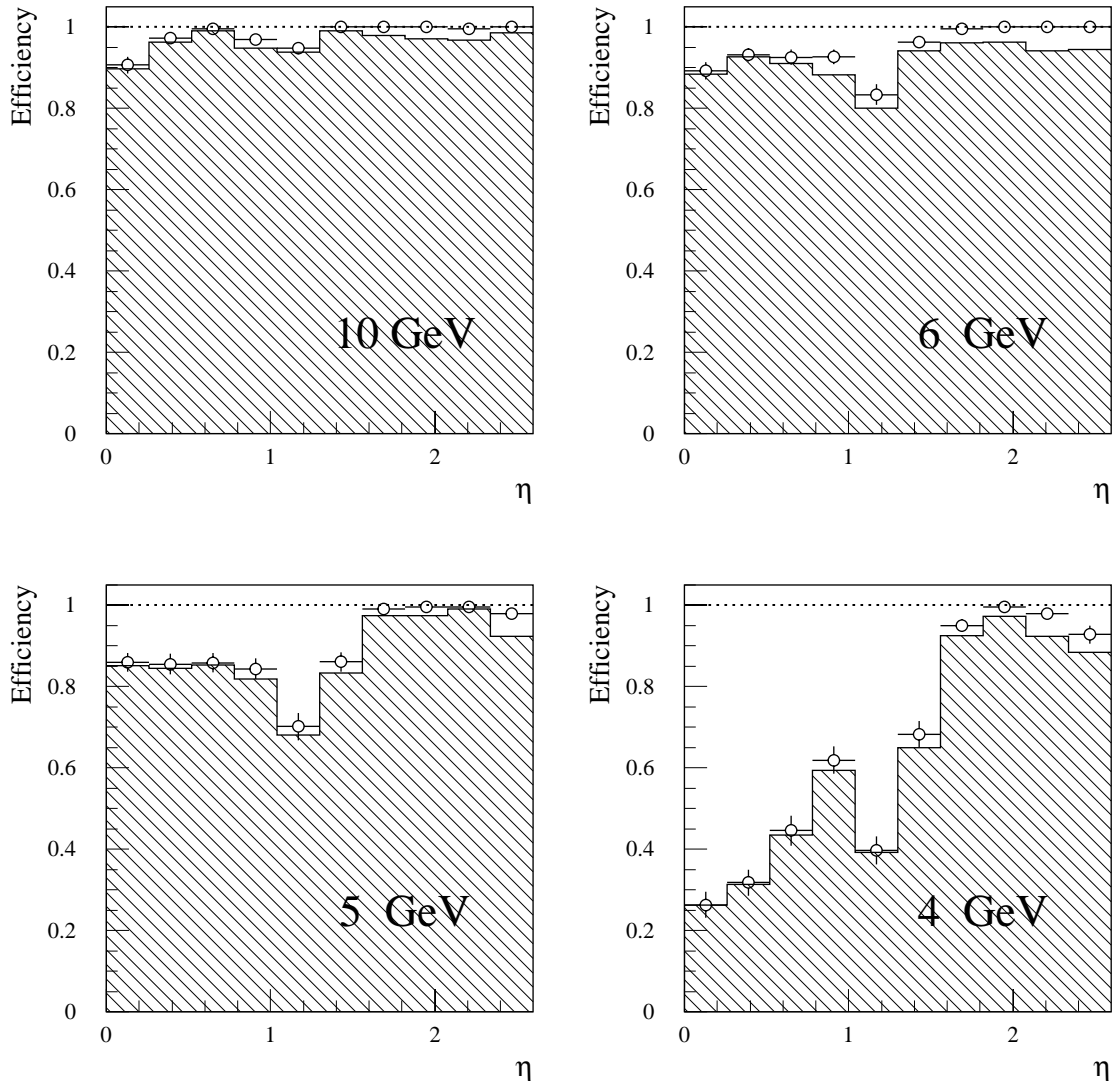
Figure 8-11 Efficiencies of track reconstruction in the Muon System (open circles) and of tracks combination (histogram) using the STACO procedure as a function of η and at different low p_T.

ments together with the Inner Detector and the Tile Calorimeter measurements (in order to have a constraint in the transverse plane) could lead to a good identification efficiency of muons with p_T as low as 3 GeV. This method remains to be studied in detail.

8.2 Identification of low p_T muons using the Tile Calorimeter

Lepton identification in the transverse momentum range from 3 GeV to 10 GeV is essential to perform the b-physics studies (see Chapter 17). As already stated in the preceding section, the muon reconstruction efficiency decreases rapidly below 6 GeV specially at low rapidity. In order to efficiently identify low p_T muons, the last sampling of Tile Calorimeter can be used. Muons with energy above 3 GeV reach this sampling and deposit energy of a minimum ionising particle while the inner samplings act as a filter for hadrons which leave very little energy on the last sampling.
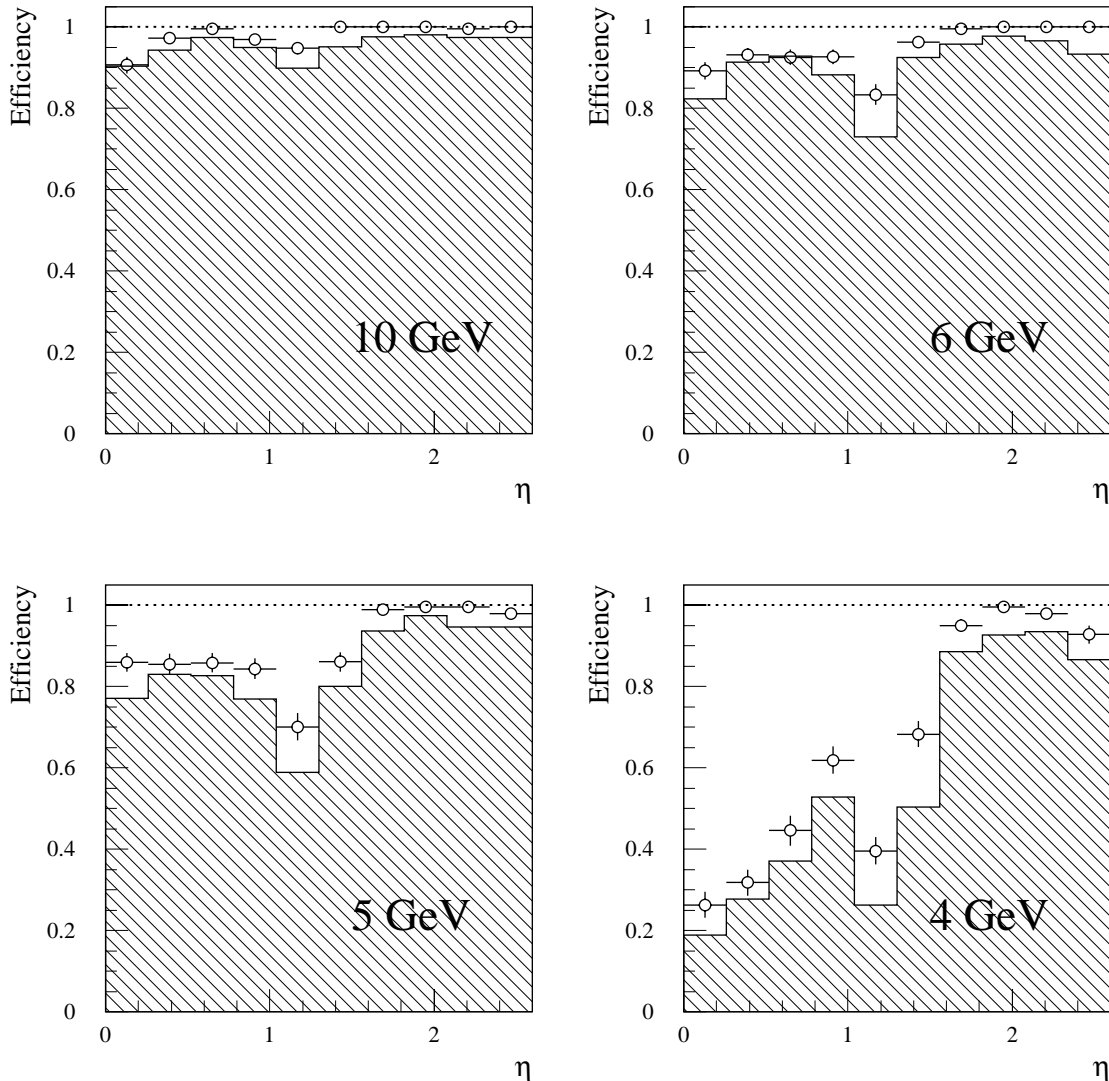
Figure 8-12 Efficiencies of track reconstruction in the Muon System and of tracks combination using the MUID procedure as a function of η and at different low p_T.

Single muons with p_T in the 3-5 GeV range were simulated in the pseudorapidity region $|\eta| < 1.5$ (in the Tile Calorimeter acceptance). Single pions with $p_T = 5$ GeV were also simulated in the same range in order to get a conservative estimate of hadron contamination.

The principle is to reconstruct tracks in the Inner Detector and to propagate those with $3 < p_T < 5$ GeV to the third hadronic sampling. Energy deposition in the calorimeter cells that are hit (on-Road cells) are recorded, as well as energy deposition in the nearest cells (off-Road cells). The most simple criteria is then to analyse the energy deposition in the last hadronic sampling. Figure 8-14 shows the distributions of these energy deposits. Selection of events with energy above 0.3 GeV gives the best results. Such selected cells can then be associated with tracks reconstructed in the Inner Detector. The tracks in a cone of R < 0.4 around the selected cells are tagged as potential muon candidates.

Figure 8-15 shows the muon identification efficiency as a function of η. The drop of efficiency for η around 0.7 is due to the gap between the barrel and extended barrel of the Tile Calorimeter; the efficiency drop at $|\eta| = 1.1$ is due to tracks crossing the extended barrel and depositing
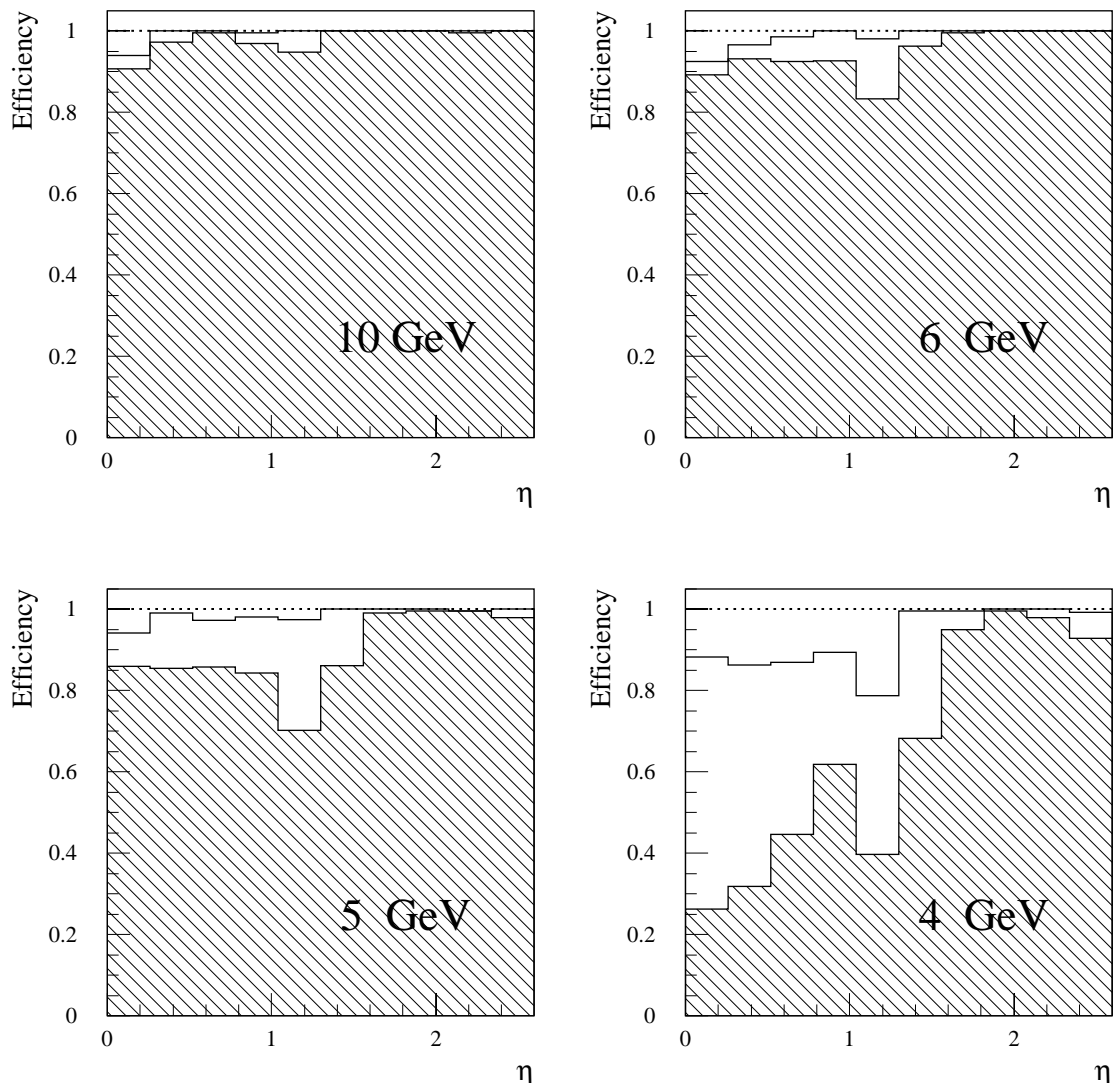
Figure 8-13 Efficiency of track reconstruction in Muon System (hatched histogram) and fraction of events with reconstructed inner stations segments (empty histogram) as a function of η and at different low p_T.

comparable amount of energy in two close cells in the third hadronic sampling. The decrease of efficiency at $\eta = 0$ is due to the large probability of muon absorption in that region. Figure 8-16 shows the probability of hadron misidentification as a function of η. Regions with low rejection occur where the amount of crossed material is minimal.

Muon detection efficiency and hadron rejection could be further improved by using other measurements as the energy deposition in the inner samplings of the Hadron Calorimeter, the energy measurement in the EM Calorimeter and the track reconstruction in the inner most stations of the Muon System
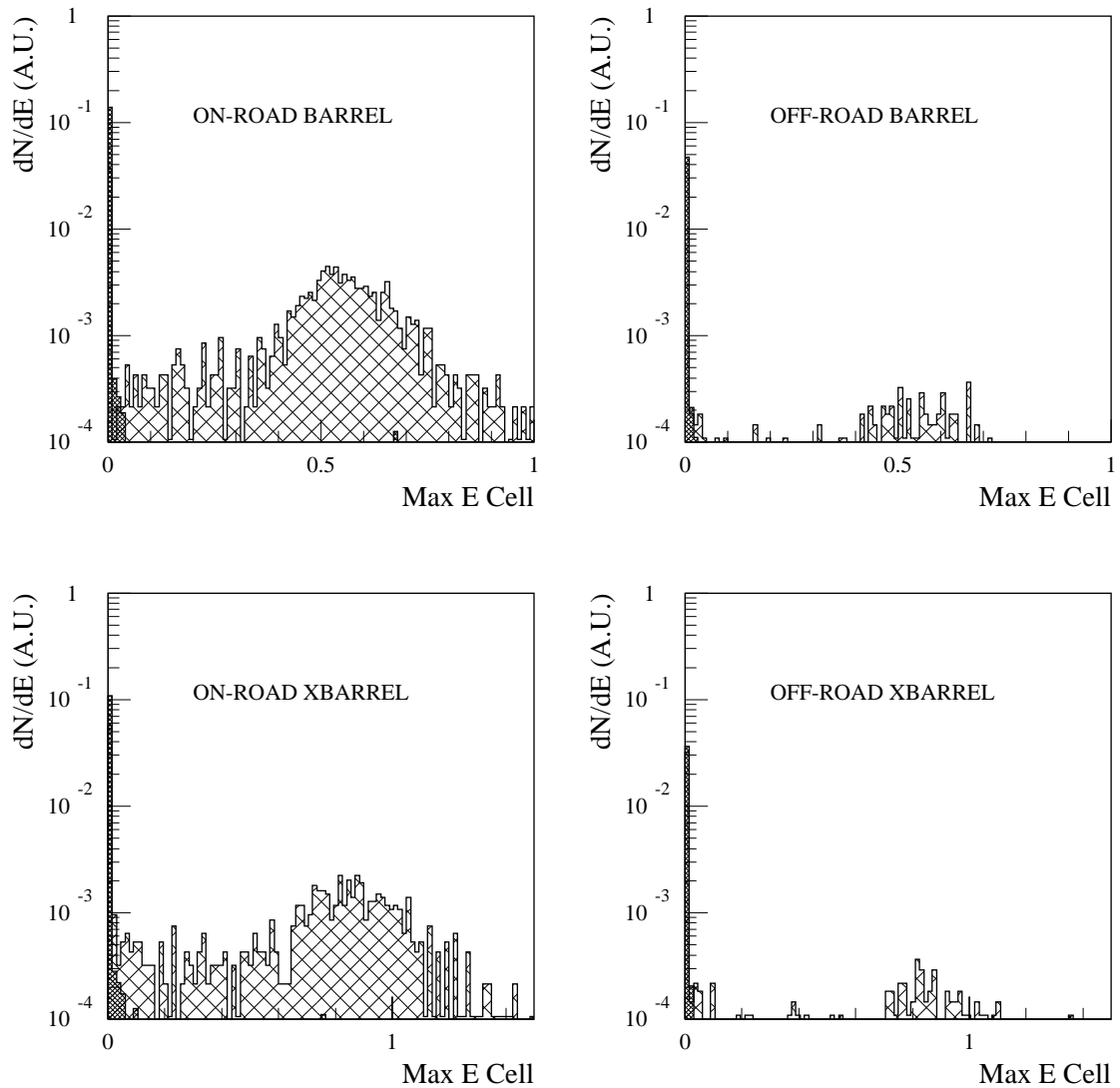
Figure 8-14 Distribution of the energy (in GeV) in on-road and off-road (see text) cells of the third sampling of the barrel Tile calorimeter (barrel and extended barrel) for 5 GeV pions (densely hatched histogram) and for 3 GeV to 5 GeV muons (hatched histogram).

8.3 Muons from π/K decays

For *B*-physics studies, the LVL1 trigger is an inclusive muon trigger with p_T threshold of 6 GeV. At low transverse momenta ($p_T < 8$ GeV) in-flight decays of π and K mesons ($\pi \to \mu\nu$ and $K \to \mu\nu$) are the dominant source of muons and thus of trigger rate in the LVL-1 Muon System. The purpose of the LVL2 muon trigger is the identification of the muon tracks using the Muon System and the extrapolation to the Inner Detector. The comparison of these tracks with those reconstructed in the Inner Detector gives a possibility to reduce the trigger rate by requiring a good match. A muon originating from π/K decay and detected by the Muon System has a momentum lower than the original meson detected in the Inner Detector. In addition, the π–μ or K–μ trajectory shows a kink where the decay occurs; as a consequence the χ^2 of the combined track is spoiled. However, the multiple scattering and energy loss fluctuations (especially in the calorimeters) dilutes this effect.
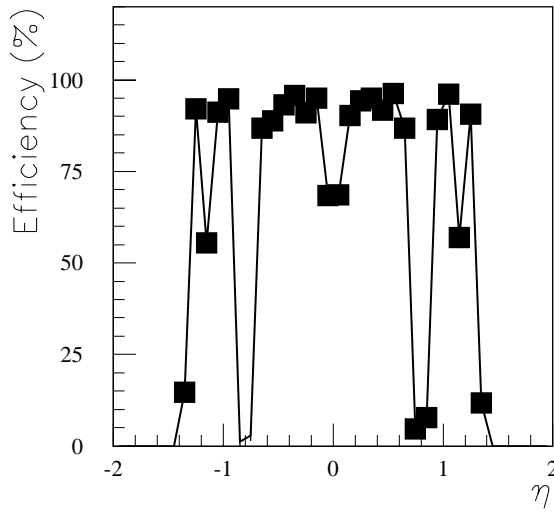
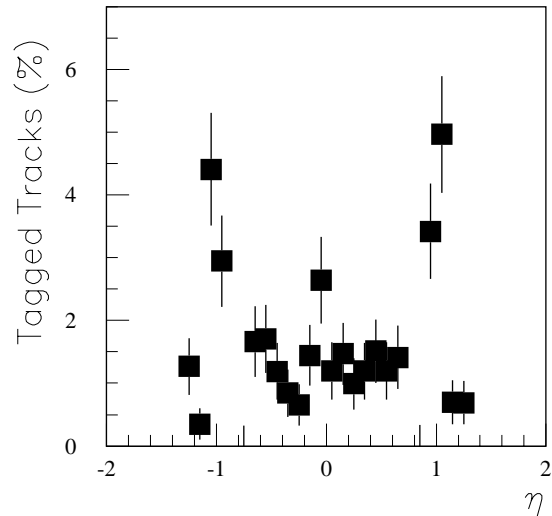**Figure 8-15**   Efficiency of selection for 3 GeV to 5 GeV muons.

Figure 8-16 Efficiency of selection for 5 GeV pions.

To estimate the rejection, non-prompt muons from π/K decays and prompt muons with fixed p_T between 6 and 12 Gev and $|\eta| < 2.5$, were simulated. The decay of π/K was limited to the maximal radius of 1.40 m. The reconstruction of charged tracks in Inner Detector has been performed using xKalman and in Muon System using MUONBOX. All tracks found in the Muon System were extrapolated to the Inner Detector.

The analysis starts by looping over all tracks reconstructed in the Muon System and it proceeds in three steps. In the first step, only muons with p_T larger than 4.2 GeV are retained. The value of this cut allows high reconstruction efficiency of prompt muons with $p_T > 6$ GeV. Figure 8-17 shows the reconstruction efficiency both for prompt and π/K decay muons. In the second step, a track is accepted if it satisfies the following cuts:

1. Number of precision hits ≥ 9.

2. Number of pixel hits ≥ 2.

3. At least one associated hit in the B-layer.

4. $|d_o| < 1$ mm, were d_o is the transverse impact parameter of the track.

5. χ^2 per degree of freedom of track fit procedure ≤ 2.

6. Number of TRT hits ≥ 20.

The first four cuts correspond to quality cuts which have been developed in the context of *b*-tagging and the last two cuts were added to enhance the rejection of non-prompt muons. Figure 8-18 shows the efficiencies after these cuts.
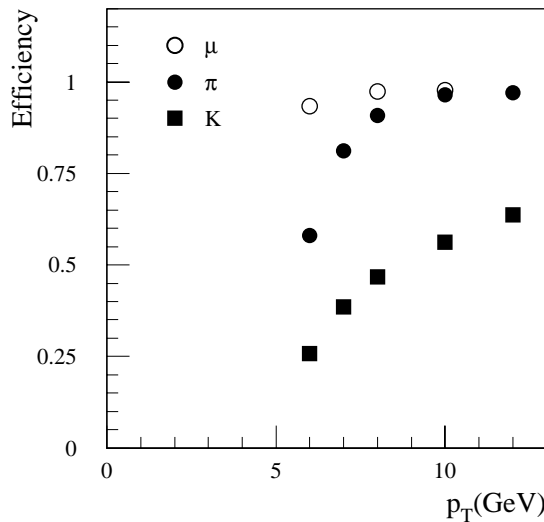
Figure 8-17 Reconstruction efficiency at first selection step (cut on p_T reconstructed the in Muon System) as a function of p_T.
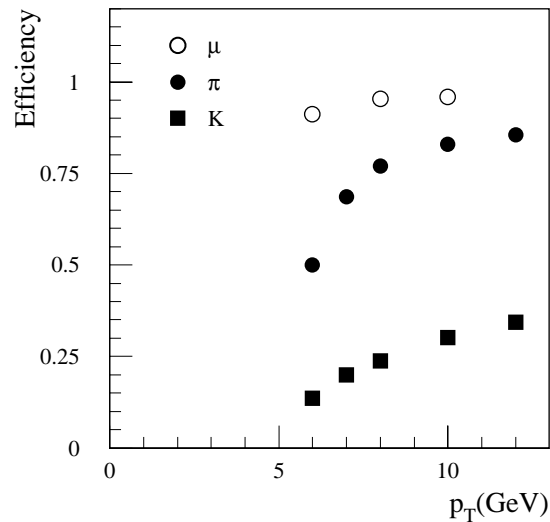

Figure 8-18 Reconstruction efficiency at second selection step (cut on quality of Inner Detector track) as a function of p_T.

Finally, the combination of the reconstructed tracks from the Inner Detector and from the Muon System is performed using the STACO procedure described in Section 8.1. Only combined tracks with χ^2 per degree of freedom less than 6 and $p_T > 5.6$ GeV are accepted.

Figure 8-19 indicates that only 10-15% of muons from K decays and 30-50% of muons from π decays were misidentified as prompt muons and that the efficiency for prompt muons is ~90% in the p_T range 6-10 GeV.

The rejection of non-prompt muons depends strongly on the distance from the beam line where the decay occurs. Figures 8-20 and 8-21 show the reconstruction efficiency of non-prompt muons originating from π/K with $p_T = 8$ Gev as a function of the decay radius after three steps of the selection algorithm.
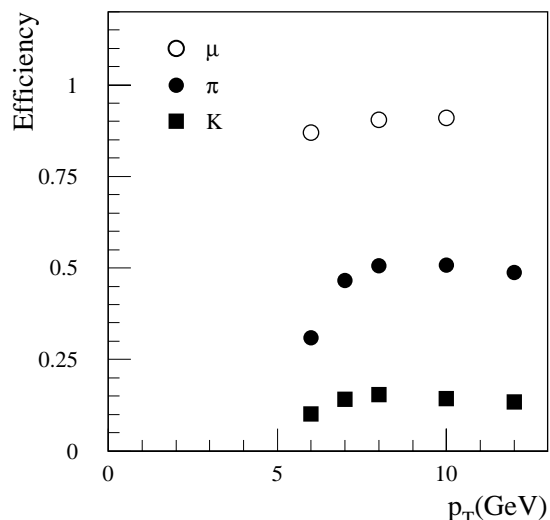

Figure 8-19 Reconstruction efficiency at third selection step (cut on matching quality) as a function of p_T.

The reconstruction efficiency after the first step of the selection does not depend on the radius of the decay. The rejection of non-prompt muons at the second step increases for decay radii between 5 and 50 to 60 cm because of the fine-granularity of the semiconductor tracking detectors. Finally the combination of Muon System and Inner Detector systems in the last selection step partially removes the non-prompt muons from decays at radii above 50 cm.
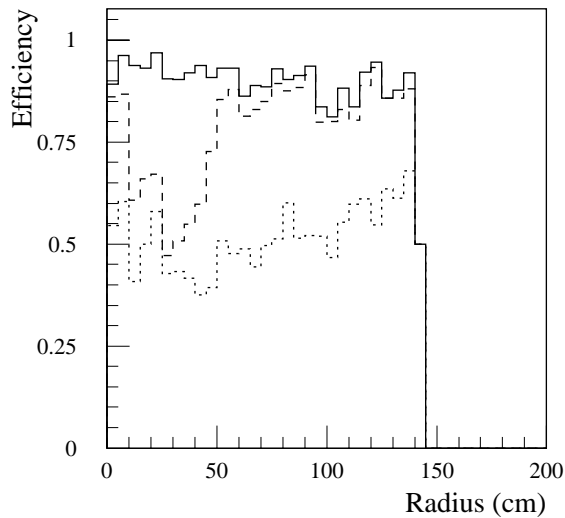
Figure 8-20 Reconstruction efficiency as a function of the radius at which the decay occurs at the different steps of the selection (solid line: first step, dashed line: second step, dotted line: last step) for the π sample.
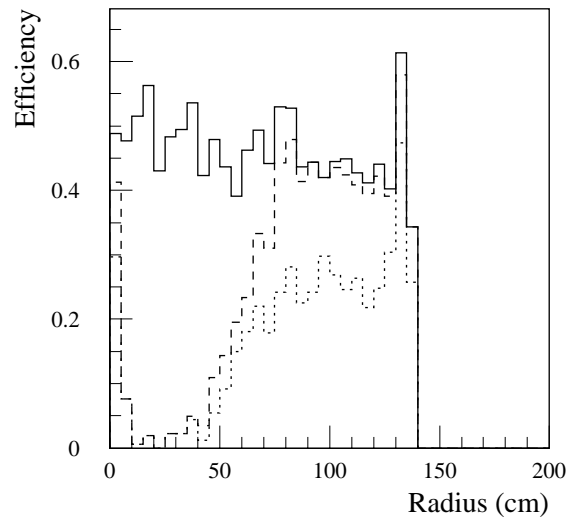
Figure 8-21 Same as Figure 8-20 but for the *K* sample.

8.4 Muons inside jets

Non-isolated muons are predominantly produced by heavy flavour (*b*- and *c*-quarks) decays. For this reason, they can be used to identify jets originating from *b*-quark fragmentation (muon *b*-tag; see Chapter 10). The main ingredients of the muon *b*-tagging are the correct muon identification and a high rejection power for decayed or misidentified hadrons.

For this investigation, muons were studied in *b*-jets produced by Higgs decays, where the Higgs mass was either 100 or 400 GeV. The STACO procedure (see Section 8.1) was used for combining the tracks measured in the Muon System and in the Inner Detector.

The overall reconstruction efficiency of muons with $p_T > 6$ GeV within the Inner Detector acceptance is 90%, which is 5% lower than that for isolated muons. Figure 8-22 shows the reconstruction efficiency as a function of p_T for muons in jets (histogram) and for single muons (triangles). The lower efficiency for non isolated muons can be attributed to the pattern recognition efficiency in the Inner Detector, and to a wrong match between the Muon System track and the Inner Detector track due to the large density of tracks in jets. The latter effect is the dominant.

Hadrons can be tagged as muons. Figure 8-23 shows the hadron misidentification probability for jets which did not contain any primary muon compared to the same probability for jets containing at least one primary muon. In the first case the misidentification is due entirely to decays in flight of pions and kaons; in the latter case the additional contribution arises from muon matching errors.

Muons with $2 < p_T < 6$ GeV and $|\eta| < 1.75$ can be tagged through their energy deposit in the outer segment of the Tile Calorimeter. Figures 8-24 and 8-25 show this energy deposit as a function of pseudorapidity, for muons and for hadrons respectively, with $p_T > 2$ GeV. Selecting only cases where the energy in the last segment was in the band limited by the dotted lines, it is possible to achieve an efficiency of 75% (85% for $|\eta| < 1.25$) with a hadron rejection factor of ~10.
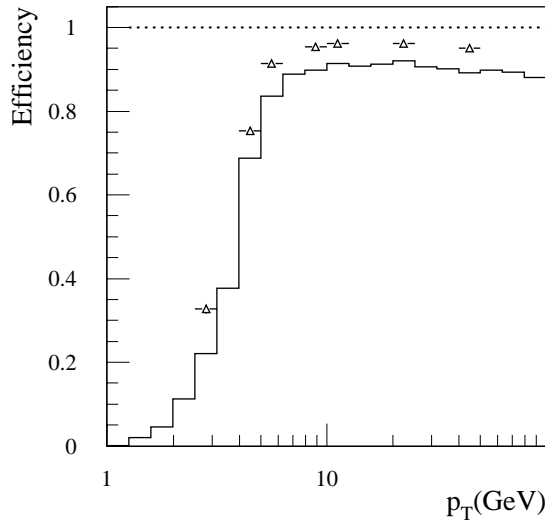
Figure 8-22 Muon reconstruction and identification efficiency as a function of p_T. The histogram is for muons in jets from Higgs decays, the open triangles are for single muons.
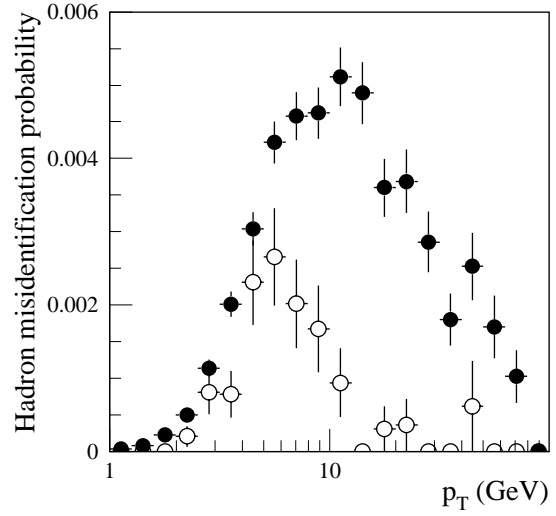
Figure 8-23 Hadron misidentification probability as a function of p_T. Full circles: hadrons in jets containing at least one primary muon. Open circles: hadrons in jets not containing primary muons.

Figure 8-26 shows the muon identification efficiency and hadron misidentification rate as a function of p_T for particles with $|\eta| < 1.75$. Figure 8-27 shows the muon identification efficiency and hadron misidentification rate as a function of pseudorapidity for particles in the range $2 < p_T < 8$ GeV.
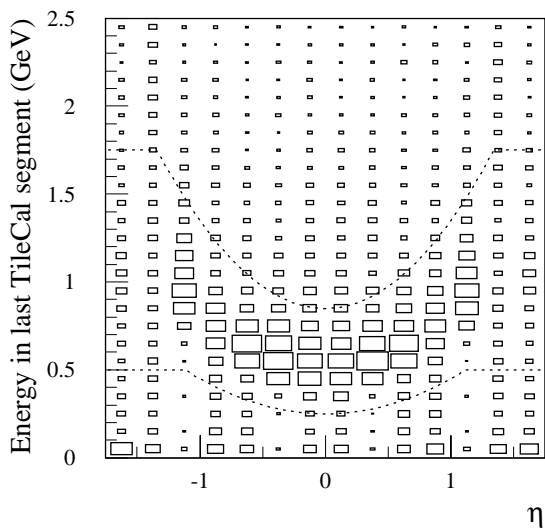

Figure 8-24 Energy deposited in the outer Tile Calorimeter segment by muons in jets as a function of pseudorapidity.
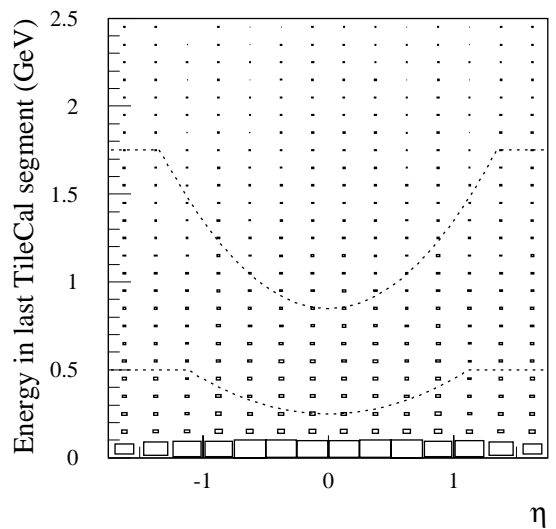
Figure 8-25 Energy deposited in the outer Tile Calorimeter segment by hadrons in jets as a function of pseudorapidity.
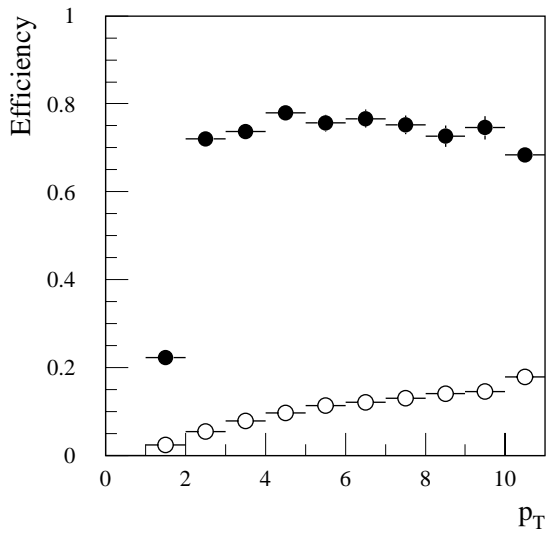
Figure 8-26 Tile Calorimeter muon identification efficiency (full circles) and fraction of misidentified hadrons (open circles) as a function of p_T for particles in jets with $|\eta| < 1.75$.
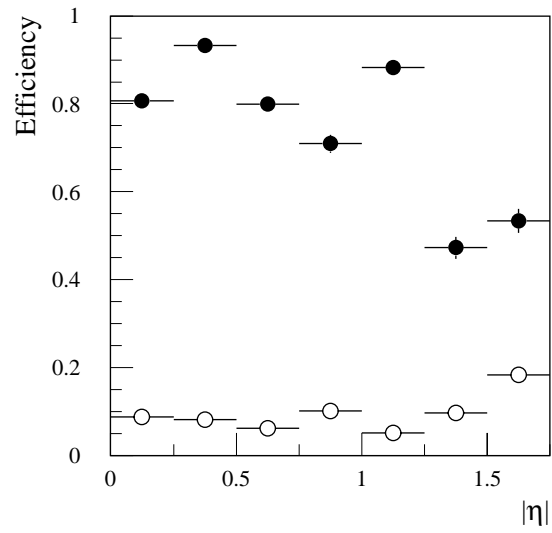
Figure 8-27 Tile Calorimeter muon identification efficiency (full circles) and fraction of misidentified hadrons (open circles) as a function of $|\eta|$ for particles in jets with $2 < p_T < 8$ GeV.

Since the cells of the last sampling are large ($\Delta\eta = 0.2$, $\Delta\phi = 0.1$), the energy entering in Figure 8-25 is not deposited by a single hadron but by several. Thus the probability for a jet to induce a muon signature cannot be simply deduced from the hadron probability shown in Figure 8-27 and the hadron multiplicity in the jet but depends on the jet topology. This method of identifying muons is also used to tag b-jets (see Chapter 10).

8.5 Muon isolation

The dominant background to the $H \rightarrow ZZ^* \rightarrow \mu\mu\mu\mu$ signal consists of four-lepton events from $t\bar{t}$ and $Zb\bar{b}$ production. In these backgrounds, at least two of the muons come from direct or cascade b-decay. Therefore they are non-isolated and one can reject them on the basis of energy deposited in the calorimeters.

For this study, muon candidates reconstructed in the Muon System have been selected. A sample of 1 500 single muons of fixed $p_T = 20$ GeV and a sample of 1 100 events $pp \rightarrow b\bar{b}X \rightarrow \mu X$, where the muon coming from the b decay is required to have a transverse momentum greater than 20 GeV, have been simulated in the detector. Electronic noise was included and pile-up was simulated by adding 2.3 (23) minimum bias events for low (high) luminosity.

Figure 8-28 shows the distribution of the transverse energy collected in the electromagnetic calorimeters cells lying in a cone of radius $R = 0.3$ around the muon direction. The energy deposit in the calorimeters around the muon direction allows to separate isolated from non-isolated muons. Figure 8-29 shows the mean value of the transverse energy collected in a cone around the reconstructed muon direction as a function of cone radius for low and high luminosity and for isolated and non-isolated muons. This plot suggests the value R = 0.3. This value is a good compromise between a large value needed to fully contain the energy from hadrons associated with non-isolated muons and a small value needed to reduce the effect of pile-up and electronics noise.
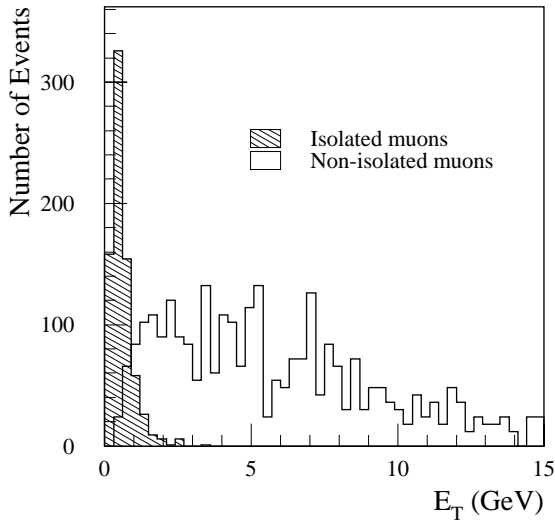
Figure 8-28 Transverse EM-energy distribution in cone of radius 0.3 around muon direction for isolated and non-isolated muons.
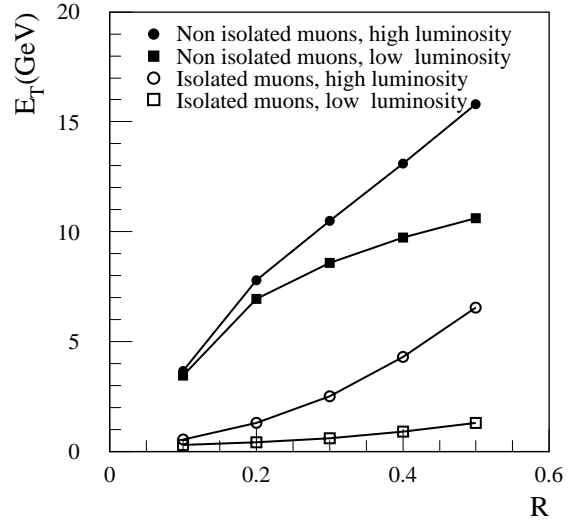

Figure 8-29 Mean value of transverse EM-energy in a cone around muon direction as a function of the cone radius R.

The contribution from pile-up, which increases with the luminosity, introduces also a pseudorapidity dependence of the transverse energy deposited in the calorimeters. This is illustrated in Figure 8-30 where the mean values of the transverse energy is plotted as a function of η. The dependence shown on this latter figure has been removed by using a weight factor in order to get a η corrected transverse energy independent of η.

A cut on the transverse energy collected in the EM Calorimeter cells in the isolation cone is applied to select the isolated muons. At high luminosity, is preferable to cut on η corrected transverse energy. Figures 8-31 and 8-32 show the selection efficiency for isolated and non-isolated muons as a function of the threshold energy for low and high luminosity. One notes that the selection efficiency for non-isolated muons depends on the luminosity and, to some extent, on the muon momentum.
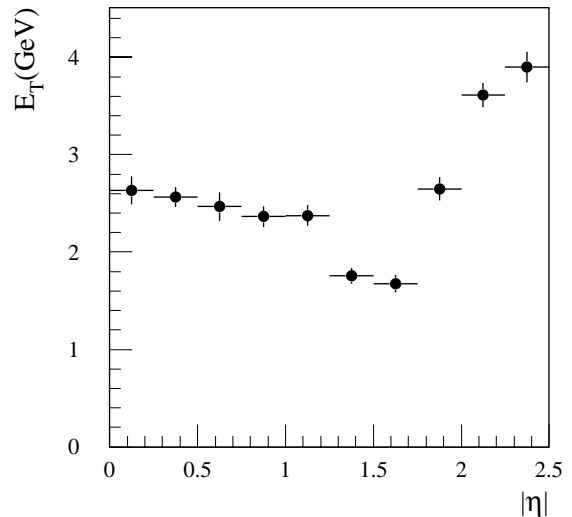

Figure 8-30 Mean value of transverse energy in a cone of radius 0.3 around the muon direction as a function of pseudorapidity for high luminosity.
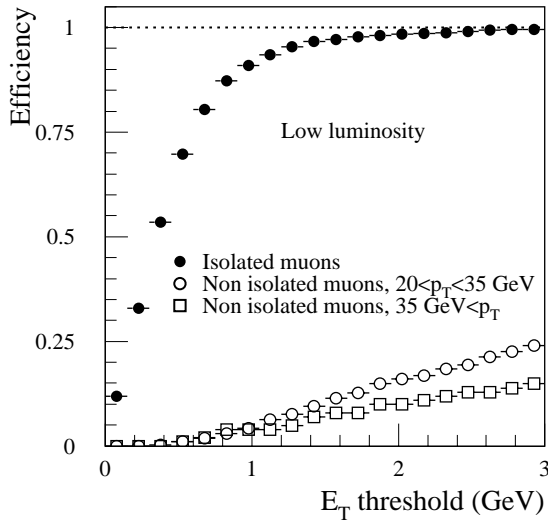
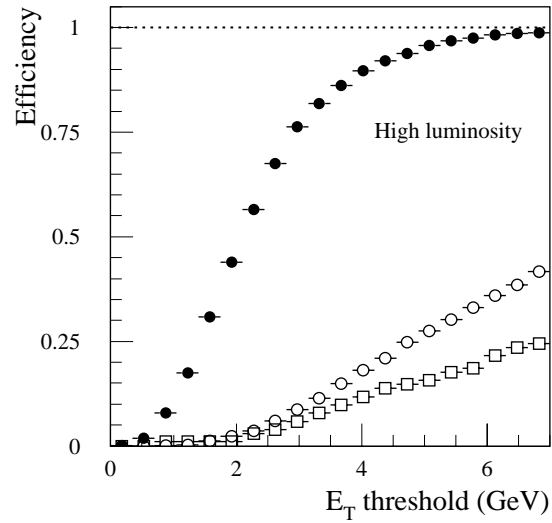**Figure 8-31** Muon selection efficiency as a function of the transverse energy threshold at low luminosity.

Figure 8-32 Muon selection efficiency as a function of the transverse energy threshold at high luminosity.

8.6 Mass and charge reconstruction

8.6.1 Reconstruction of $Z \rightarrow \mu\mu$

The process $Z \rightarrow \mu\mu$ is a high-statistics control sample which will be used for detector calibration and monitoring of the detector performance. A sample of events has been generated with PYTHIA 5.7 [8-7] and PHOTOS 2.0 [8-8] in order to include inner bremsstrahlung. Figure 8-33 shows the reconstructed Z mass using MUONBOX. A Gaussian fit (within a 2σ window) gives $\sigma = 3.0$ GeV, of which about 1.9 GeV comes from the natural width; the measurement accuracy contributes with an error of 2.0 GeV.

The mass resolution can be improved by combining the measurements from the Muon System and from the Inner Detector. The combined reconstruction has been performed using the STACO procedure. The combined reconstructed mass is shown in Figure 8-34. A Gaussian fit gives $\sigma = 2.5$ GeV.

8.6.2 Dimuon final state

If the MSSM parameter $\tan\beta$ is large enough, the process $H/A \rightarrow \mu\mu$ becomes detectable (see Section 19.3.2.6). The most critical issue in the detection of such a particle in the few hundred GeV mass range is the suppression of the very large dimuon background. There are two main sources of opposite-sign dimuons, namely the Drell-Yan processes and $t\bar{t}$ production. It has been shown that this background is very high and therefore the mass resolution is crucial to isolate the signal [8-11].

A sample of $A \rightarrow \mu\mu$ have been simulated for two higgs masses: 150 GeV and 300 GeV. The event reconstruction has been performed using the MUID procedure described in Section 8.1.
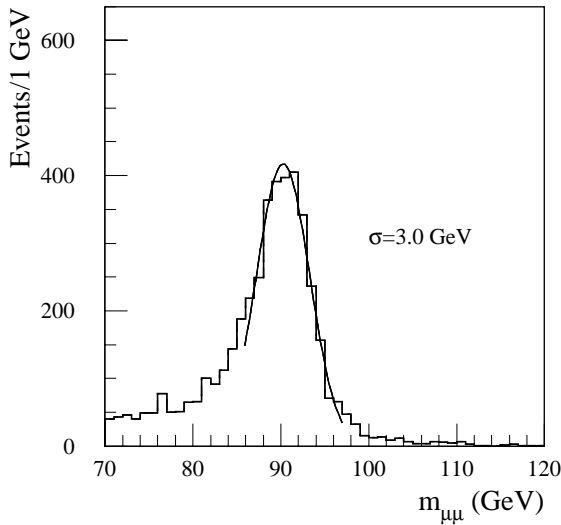
Figure 8-33 Distribution of the reconstructed *Z* mass using the standalone Muon System.
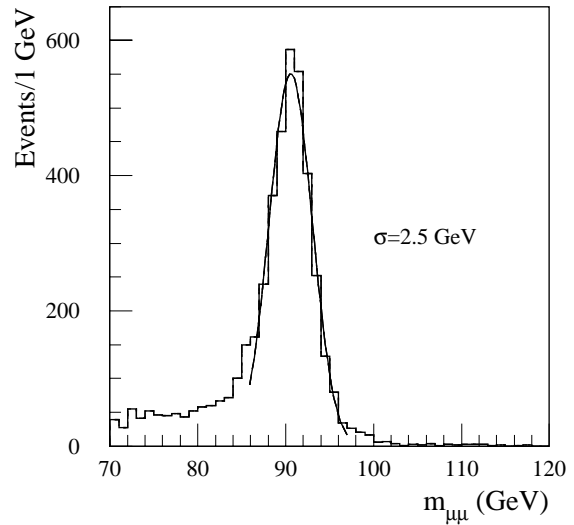

Figure 8-34 Distribution of the reconstructed *Z* mass using the combined information from the Muon System and the Inner Detector.
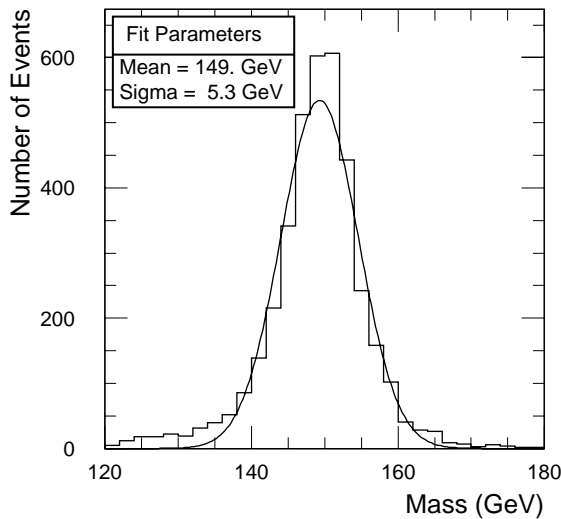

Figure 8-35 Distribution of the reconstructed dimuon invariant mass for an *A* with a mass of 150 GeV using the Inner Detector only.
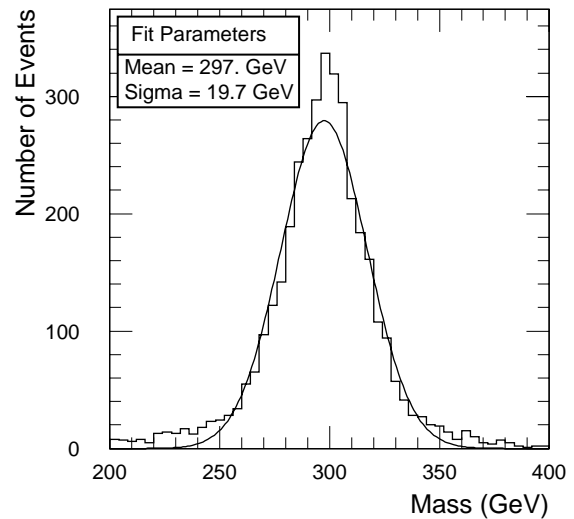

Figure 8-36 Distribution of the reconstructed dimuon invariant mass for an *A* with a mass of 300 GeV using the Inner Detector only.

The reconstructed invariant mass is shown in Figures 8-35, 8-36, 8-37 and 8-38 when the Muon System and the Inner Detector are used separately. The low mass tails in these mass distributions come from inner bremsstrahlung. The result of combined muon reconstruction is shown in Figures 8-39 and 8-40; with respect to the standalone Muon System reconstruction, the mass resolution is improved by about 25% at low mass and 10% at high mass. The dependence on the mass of this improvement reflects the higher p_T of the decay muons. The signal-to-background ratio achievable with this mass resolution is presented in Section 19.3.2.6.

The dimuon mass resolution is also of interest at high mass, where new neutral heavy bosons are possible. A study of the 3 Tev Z' decaying to two muons yields a mass resolution of 8% [8-11].
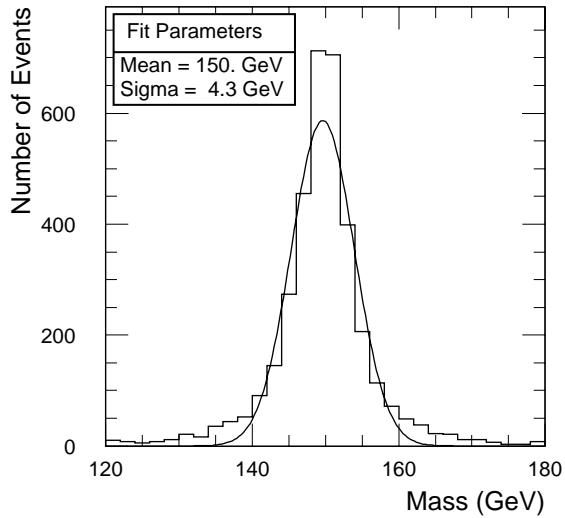
Figure 8-37 Distribution of the reconstructed dimuon invariant mass for an *A* with a mass of 150 GeV using the Muon System only.
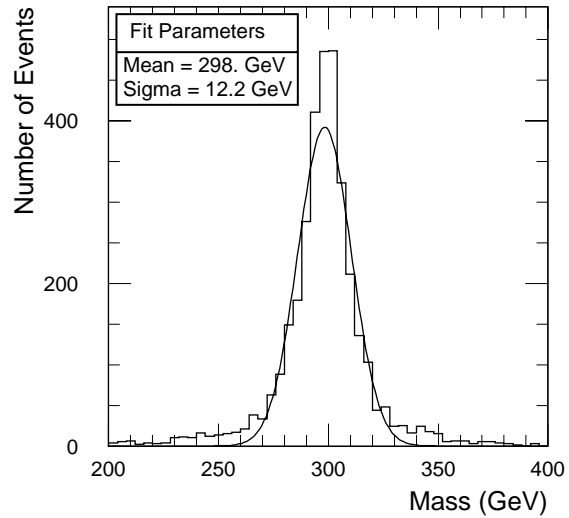

Figure 8-38 Distribution of the reconstructed dimuon invariant mass for an *A* with a mass of 300 GeV using the Muon System only.
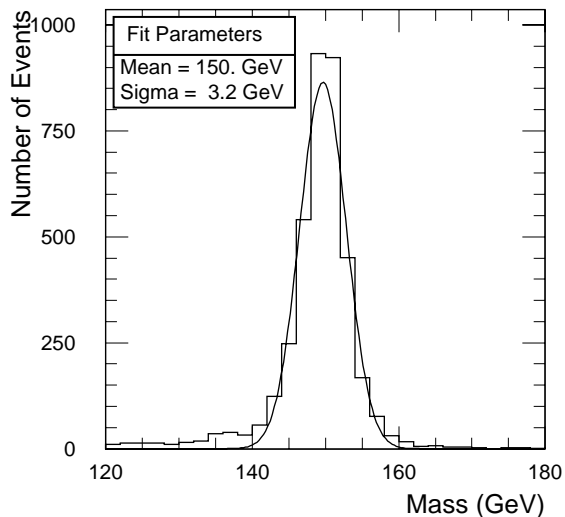

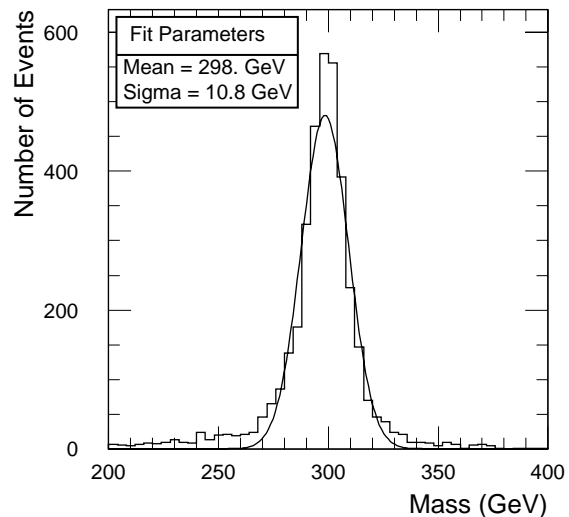**Figure 8-39** Dimuon invariant mass distribution for 150 GeV *A* using combined reconstruction.

Figure 8-40 Dimuon invariant mass distribution for 300 GeV *A* using combined reconstruction.

8.6.3 Four-muon final state

The SM Higgs decay $H \to ZZ^* \to \mu\mu\mu\mu$ has been studied extensively. Details of the event selection can be found in Section 19.2.5. The typical reconstruction efficiency of these events using the Muon System is ~85% for masses greater than 130 GeV (see Table 8-1). This and the following reconstruction efficiencies are normalised to the number of events with all decay muons in the η region $|\eta| < 2.5$. Table 8-1 shows the four-muon mass resolution as a function of the simulated Higgs mass. When only the Muon System is used for the event reconstruction, the measurement accuracy ranges from 2.7 GeV to 4.7 GeV for the mass range from 130 to 200 GeV. This result is obtained with a Gaussian fit in a 2σ interval centred on the peak of the distribution. Table 8-1 shows also the fraction of events that are reconstructed within this interval.

The combination of the Muon System and Inner Detector measurements improves the mass measurement. Figure 8-41 shows the reconstructed mass distribution for 130 GeV Higgs decays using the standalone Muon System, the Inner Detector and combining the two systems. The study has been performed using the STACO procedure. Table 8-1 shows that the mass resolution is improved by about 30-40% and that the non-Gaussian tails are reduced; therefore the detection sensitivity is increased.

Table 8-1 Reconstruction efficiency, mass resolution without/with the *Z* mass constraint and size of tails for different Higgs masses using the combined information and standalone measurement including bremsstrahlung.

Higgs mass (GeV)	Reconstruction efficiency in %	σ Muon System (GeV)	σ Inner Detector (GeV)	σ Combined (GeV)	% of tails Combined
130	83.6	2.7/2.1	1.8/1.6	1.6/1.4	17.5
170	84.7	3.6/3.1	2.4/2.1	2.1/2.0	16.8
200	85.3	4.7/4.0	3.5/3.0	3.1/2.9	20.2

In the Higgs search, the kinematic constraint of the Z mass improves the mass resolution. The Z mass constraint was applied when the mass of muon pair was within 6 GeV of the Z mass. Figure 8-41 shows the reconstructed mass distribution for $m_H = 130$ GeV after constraining one muon pair to the Z mass. Table 8-1 shows that the improvement is of about 20%, when the mass resolution is dominated by the instrumental precision. If the resolution is close to the natural Z width, the improvement becomes less than 20%. The breakdown of the about 17% of tails at $m_H = 130$ GeV is, in addition to the expected 5% in the Gaussian case, 5% from events for which the reconstructed Z mass is more than 6 GeV from the nominal Z mass, 4% from events with bremsstrahlung and 3% from muon reconstruction tails.

Table 8-2 Same as Table 8-1 but without bremsstrahlung.

Higgs mass (GeV)	Reconstruction efficiency in %	σ Muon System (GeV)	σ Inner Detector (GeV)	σ Combined (GeV)	% of tails Combined
130	83.7	2.6/2.0	1.7/1.5	1.4/1.3	14.0
170	84.7	3.4/2.9	2.2/2.0	2.0/1.8	14.4
200	85.3	4.5/3.7	3.2/2.7	2.8/2.4	18.9

Table 8-2 shows again the reconstruction efficiency, the mass resolution and the size of tails for event without taking into account the contribution of the bremsstrahlung as it has been done for the Muon TDR [8-9] and in [8-10]. The present results are consistent with those presented in these documents.

8.6.4 Muon charge identification

Charge identification is essential for a wide range of physics topics. Examples are the measurement of CP violation using the charge of the muon to tag the B^0 or $\overline{B}^0$ production; search for strongly interacting Higgs by detecting the same-sign *W*-pairs; search for supersymmetric particles by looking for same-sign dileptons, and charge asymmetry measurement to determine the property of new gauge boson couplings. The Muon System provides excellent charge identification covering the full range of the muon momenta for the above physics processes.
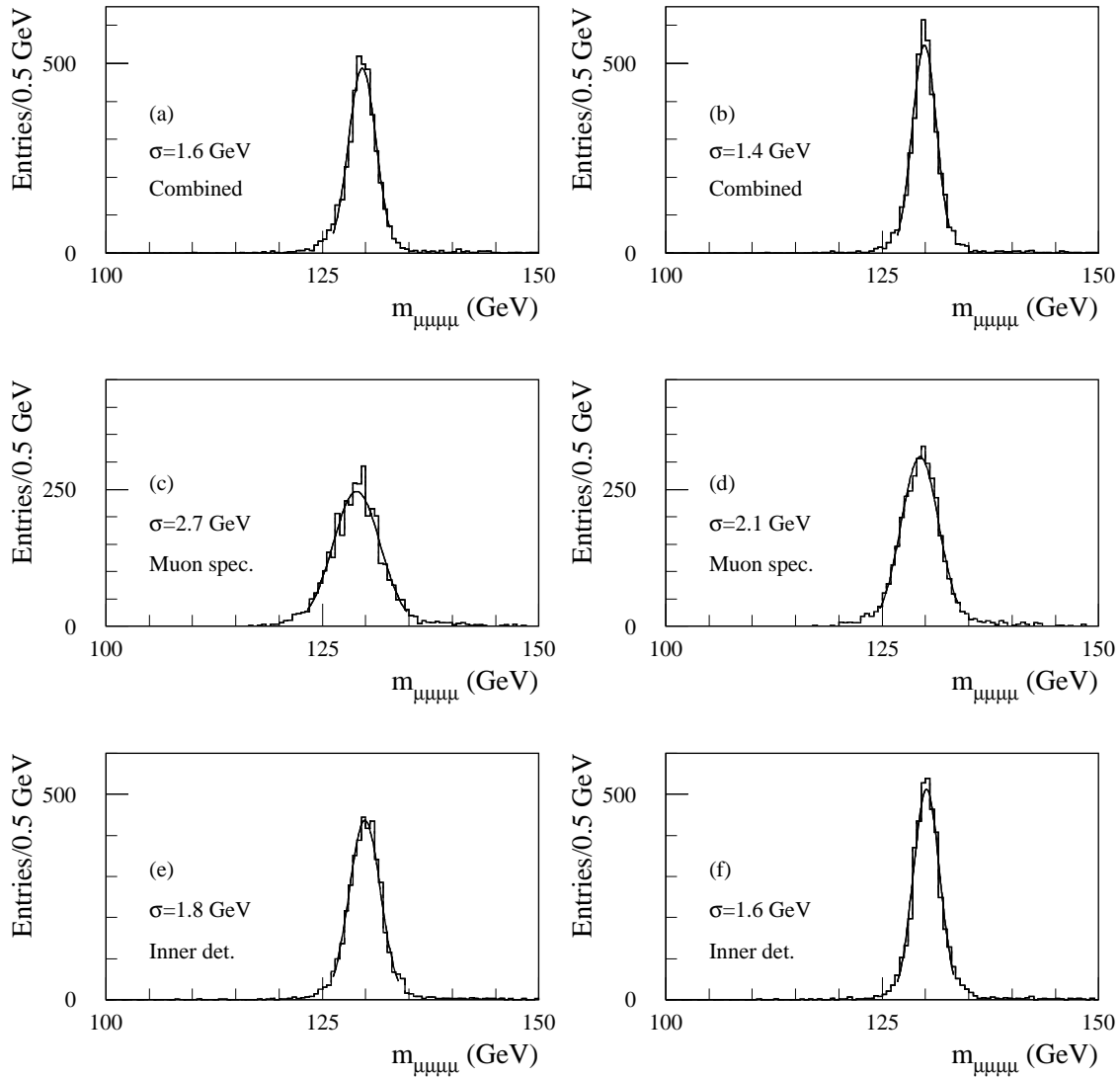
Figure 8-41 Reconstructed mass distribution for the Higgs decay $H^0 \to ZZ \to \mu^+\mu^-\mu^+\mu$ (130 GeV) using the combined information (a), standalone Muon System (c), and Inner Detector (e) without applying a Z constraint and with applying a Z constraint (b), (d), and (f). Inner bremsstrahlung has been taken into account.

As an example, $W' \to \mu\nu$ events simulated and reconstructed with the Muon System reconstruction program have been studied [8-11]. The probability of charge misidentification is determined by the ratio of the reconstructed muon events with the wrong charge determination to the total numbers of reconstructed events. The charge misidentification probability as a function of the W' mass is shown in Figure 8-42. The probability of charge misidentification for a W' of 1 TeV mass is in the range of 0.2% to 0.9%. Even at a W' mass of 6 TeV, the charge misidentification probability is below 4%.
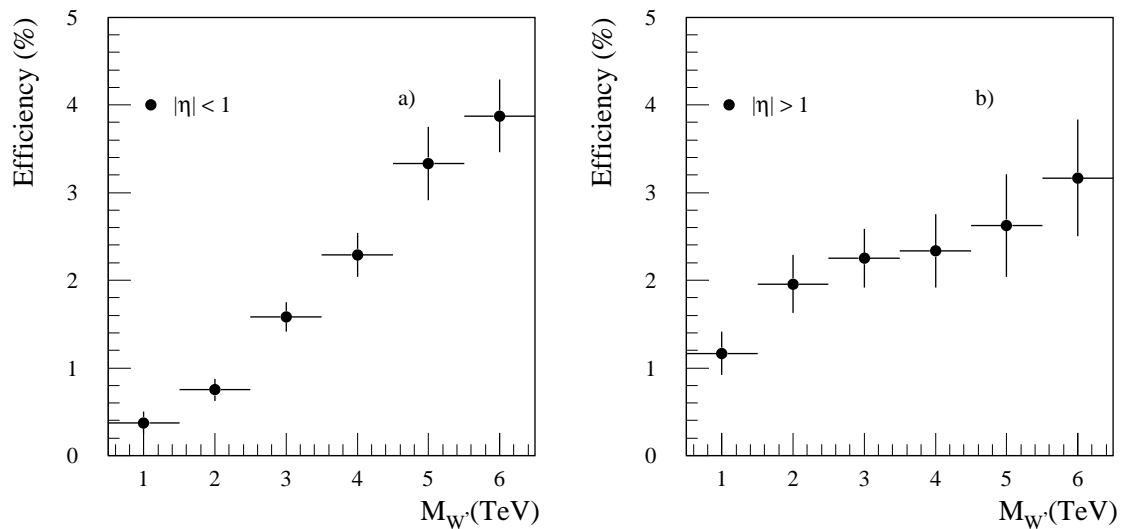
Figure 8-42 Charge misidentification probability for barrel a) and end-cap regions b).

8.7 Conclusion

The ATLAS combined muon measurements provide a highly performant muon reconstruction in a very large momentum range. The global reconstruction based on information from the Inner Detector and the Muon System allows the reconstruction of high energy muons with p_T from 6 GeV up to the limit of the muon spectrometer ($p_T \sim 2$ TeV); the reconstruction efficiency is better than 85%. The correct matching of Muon Spectrometer and Inner Detector tracks allows rejection of background muons, such as those produced in π/K decays, and allows identifying muons correctly in heavy-flavoured jets. Muons with p_T below 6 GeV can be efficiently identified and measured combining the Inner Detector track reconstruction with the energy clusters available in the Tile Calorimeter, using the last compartment to recognise muon tracks.

The accurate momentum reconstruction in a large energy range permits a precise invariant mass measurement of multi-muon final states. The Z-boson mass is reconstructed with a resolution of 2.5 GeV, comparable with the intrinsic width; Higgs decays to four muons are reconstructed with a mass resolution of about 1.1% for Higgs masses below 200 GeV.

8.8 References

8-1   I. Gavrilenko, 'Description of Global Pattern Recognition Program (xKalman)', ATLAS Internal Note, ATL-INDET-97-165 (1997).

8-2   M. Virchaux *et al.*, 'MUONBOX: a full 3D tracking program for Muon reconstruction in the ATLAS Muon Spectrometer', ATLAS Internal Note, ATL-MUON-97-198 (1997).

8-3   R. Clifft and A. Poppleton, 'iPatRec: Inner Detector pattern-recognition and track-fitting', ATLAS Internal Note, ATL-SOFT-94-009 (1994).

8-4   CERN Program Library W5013-E, July 1991.

8-5   V. Innocente and E. Nagy, Nucl. Instr. and Meth. **A324**, (1993) 297.

8-6   W. Lavrijsen, PhD Thesis, to be published.

8-7   T. Sjostrand, PYTHIA 5.7 and JETSET 7.4, CERN-TH.7112/93.

8-8   E. Barberio and Z. Was, CERN TH 7033/93.

8-9   ATLAS collaboration, Muon Spectrometer Technical Design Report, ATLAS TDR 10,
           CERN/LHCC/97-22 (1997).

8-10   L. Poggioli *et al.*, 'Detection sensitivity for intermediate mass Higgs through muon final
           state with the ATLAS detector', ATL-PHYS-98-116 (1998).

8-11   J. Shank *et al.*, 'Studies on *A⁰, Z'* and *W'* with ATLAS Muon Detector', ATLAS Internal
           Note, ATL-MUON-97-161 (1997).

8-12   CDF II Detector Technical Design Report, Fermilab-Pub-96/390-E.